

## Electronic structure of $ACu_3Co_4O_{12}$ ( $A = Y, La, Bi$ ): Synthesis, characterization, core-level spectroscopies, high-pressure application, and *ab initio* calculation

Yuta Kato,<sup>1</sup> Meng-Jie Huang<sup>2</sup>, Keito Kasebayashi,<sup>3</sup> Takateru Kawakami,<sup>4</sup> Tatsuya Yamaguchi<sup>5</sup>, Jens Buck,<sup>6,7</sup> Ru-Pan Wang,<sup>8</sup> Matthias Kalläne,<sup>6,7</sup> Kai Rossnagel<sup>2,6,7</sup>, Peter Nagel,<sup>9,10</sup> Stefan Schuppler,<sup>9,10</sup> Yoshihiro Takahashi,<sup>5</sup> Takao Odake,<sup>1</sup> Shogo Kawaguchi,<sup>11</sup> Ikuya Yamada,<sup>12</sup> and Atsushi Hariki<sup>5</sup>

<sup>1</sup>Department of Materials Science, Graduate School of Engineering, Osaka Prefecture University, 1-1 Gakuen-cho, Nakaku, Sakai, Osaka 599-8531, Japan

<sup>2</sup>Deutsches Elektronen-Synchrotron DESY, 22607 Hamburg, Germany

<sup>3</sup>Department of Physics and Electronics, Graduate School of Engineering,

Osaka Prefecture University, 1-1 Gakuen-cho, Nakaku, Sakai, Osaka 599-8531, Japan

<sup>4</sup>Department of Physics, College of Humanities and Sciences, Nihon University, Setagaya, Tokyo 156-8550, Japan

<sup>5</sup>Department of Physics and Electronics, Graduate School of Engineering,

Osaka Metropolitan University, 1-1 Gakuen-cho, Nakaku, Sakai, Osaka 599-8531, Japan

<sup>6</sup>Institut für Experimentelle und Angewandte Physik, Christian-Albrechts-Universität zu Kiel, Germany

<sup>7</sup>Ruprecht Haensel Laboratory, Kiel University and DESY, Kiel 24098, Germany

<sup>8</sup>Department of Physics, University of Hamburg, 22761 Hamburg, Germany

<sup>9</sup>Institute for Quantum Materials and Technologies (IQMT), Karlsruhe Institute of Technology (KIT), 76021 Karlsruhe, Germany

<sup>10</sup>Karlsruhe Nano and Micro Facility (KNMF), Karlsruhe Institute of Technology (KIT), 76344 Eggenstein-Leopoldshafen, Germany

<sup>11</sup>Japan Synchrotron Radiation Research Institute (JASRI), 1-1-1 Kouto, Sayo-cho, Sayo-gun, Hyogo 679-5198, Japan

<sup>12</sup>Department of Materials Science, Graduate School of Engineering,

Osaka Metropolitan University, 1-1 Gakuen-cho, Nakaku, Sakai, Osaka 599-8531, Japan



(Received 21 December 2022; revised 11 May 2023; accepted 1 June 2023; published 11 July 2023)

We present a comprehensive experimental and computational study on A-site ordered perovskite oxides  $YCu_3Co_4O_{12}$ ,  $LaCu_3Co_4O_{12}$ , and  $BiCu_3Co_4O_{12}$  including synthesis, transport, and magnetic characterization, high-pressure application, K- and L-edge x-ray absorption spectroscopy (XAS), Co 2p core-level x-ray photoemission spectroscopy and density-functional theory (DFT) calculations combined with dynamical mean-field theory (DMFT) and +U scheme. An insulating behavior with a valence state of  $A^{3+}Cu_3^{\sim 3+}Co_4^{\sim 3+}O_{12}^{2-}$  is found for the three compounds at ambient and high-pressure conditions (up to  $\sim 55$  GPa). A DFT calculation for  $YCu_3Co_4O_{12}$  uncovers the energetics of the Cu–O and Co–O bonding formation and crystal-field splitting, leading to a narrow-gap electronic structure with a hybrid orbital and element character near the Fermi energy. The stable low-spin configuration of the Co ion is studied in comparison to a canonical perovskite cobaltite  $LaCoO_3$ . A DFT + DMFT analysis of the Cu spin-correlation function indicates that the Zhang-Rice singlet description for the  $CuO_4$  plaquette is valid, while a hybridization with the Co 3d orbitals also contributes to the Cu spin screening. The presence of the hybridization between the Co and Cu orbitals is shown by the DFT + DMFT analysis for the Co  $L_{2,3}$  XAS experimental spectra that exhibit unusual broad line shape. An increasing behavior of electrical resistance at elevated pressures is observed in all compounds and is interpreted based on a DFT + U simulation.

DOI: [10.1103/PhysRevMaterials.7.073401](https://doi.org/10.1103/PhysRevMaterials.7.073401)

### I. INTRODUCTION

A-site ordered perovskite oxides  $AA'_3B_4O_{12}$  host a variety of physical properties ranging from colossal magnetoresistance, negative thermal expansion, and metal-insulator transition [1–4]. In canonical perovskite oxides  $ABO_3$ , the A-site ion such as alkaline-earth or rare-earth element is an inactive space filter and carrier donor. In A-site ordered ones  $AA'_3B_4O_{12}$ , the A'-site ion plays an active role, adding dynamic charge and spin degrees of freedom to the low-energy physics. In the  $ACu_3B_4O_{12}$  (see Fig. 1 for the crystal structure), a divalent  $Cu^{2+}$  ( $3d^9$ ) ion serves as a fluctuating spin of  $S = \frac{1}{2}$  which couples with the B-site spins, leading to a variety of long-range magnetic orderings [2,3,5] or rarely a

Kondo effect [6,7]. When the Cu ion is trivalent ( $3d^8$ ), the Cu 3d  $xy$  state (Fig. 1) strongly hybridizes with the nearest-neighbor O 2p states, positioning its Cu–O antibonding level near the Fermi energy  $E_F$ . Then, the Cu–O antibonding level receives electrons from the B site, depending on the d level energies. Thus, this peculiar setup may cause a valence transition with a charge transfer between the Cu and B sites, which was absent in parent  $ABO_3$  perovskites and other cuprates. Such an example is  $LaCu_3Fe_4O_{12}$  that shows a charge transfer at  $T = 393$  K from Fe to Cu ions:  $3Cu^{3+} + 4Fe^{3+} \rightleftharpoons 3Cu^{2+} + 4Fe^{3.75+}$  accompanied by a negative thermal expansion, metal-to-insulator and magnetic transition [2,8,9].

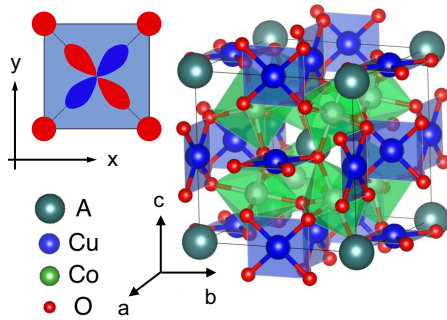


FIG. 1. Crystal structure of  $ACu_3Co_4O_{12}$  (space group:  $Im\bar{3}$ ) visualized by VESTA [10]. The indigo blue, blue, green, and red spheres represent A (=Y, La, Bi), Cu, Co, and O atoms, respectively. Single  $CuO_4$  unit and the Cu  $xy$  orbital shape are schematically shown.

In this paper, we examine  $ACu_3Co_4O_{12}$  ( $A = Y, La, Bi$ ) including synthesis, transport, and magnetic characterization, high-pressure application, x-ray absorption spectroscopy (XAS), x-ray photoemission spectroscopy (XPS) measurements, and density-functional theory (DFT) calculations.  $YCu_3Co_4O_{12}$  (YCCO) is a nonmagnetic insulator with a narrow gap and valence state of  $Y^{3+}Cu_3^{3+}Co_4^{3+}O_{12}^{2-}$ , which was studied in Ref. [11] and recently in Refs. [12,13]. A hole doping by replacing  $Y^{3+}$  with  $Ca^{2+}$  injects the carriers into the Co ( $Co^{3+} \rightarrow Co^{3.25+}$ ), while the Co ions remain in the low-spin state ( $S = 0$ ). This is in contrast with typical low-spin perovskite cobaltites, e.g.,  $La_{1-x}Sr_xCoO_3$ , where a hole doping often leads to Co spin-state transition from the undoped low-spin to a doped high-spin ( $S = 2$ ) or an intermediate-spin ( $S = 1$ ) state [14–17]. In low-spin perovskite cobaltites, e.g.,  $LaCoO_3$ , the ionic (semiconducting) gap between the filled Co  $3d t_{2g}$  and  $e_g$  states is usually small [18,19]. However, an electron doping to YCCO by substituting  $Y^{3+} \rightarrow Ce^{4+}$  changes the Cu valence ( $Cu^{3+} \rightarrow Cu^{\sim 8/3+}$ ) [13] but it does not alter the Co valence nor its spin state. This implies that the Cu–O antibonding level is positioned close to  $E_F$  and serves as an active carrier acceptor. This asymmetry in the electron and hole doping as well as the robust Co spin state highlights the unique electronic structure of this Cu–Co complex perovskite. These observations pose a question about the element and orbital character as well as the energetics on the low-energy electronic structure near  $E_F$ , and a possible charge transfer physics in the  $ACu_3Co_4O_{12}$  family.

Furthermore, the Zhang-Rice singlet physics can be explored in this Cu–Co complex system. The Zhang-Rice singlet many-body state, a hole on the Cu site ( $d^9$ ) is coupled antiferromagnetically with a doped hole on the ligand site (denoted as  $\bar{L}$ ), was introduced as a natural quasiparticle in hole-doped cuprates [20]. The Zhang-Rice singlet is stable across a wide doping range in the superconducting cuprates [21]. It is also important for understanding the first ionization state in undoped cuprates [22]. It was proposed that the Zhang-Rice singlet state is stabilized on the  $CuO_4$  plaquette in the  $ACu_3Co_4O_{12}$  system [23,24]. Previous Cu  $L_3$ -edge XAS for  $CaCu_3Co_4O_{12}$  [24] and XPS studies for  $CaCu_3Co_4O_{12}$  and YCCO [23] suggest a  $d^9\bar{L}$  character of the ground state. To further support the formation of the Zhang-Rice state, a theoretical study of the Cu spin dynamics as well as the

hybridization effect of the Cu with the Co  $3d$  states will be valuable since the hybridization with Co may dissociate the Zhang-Rice singlet from the  $CuO_4$  plaquette.

In this work, we newly synthesize  $LaCu_3Co_4O_{12}$  (LCCO) and  $BiCu_3Co_4O_{12}$  (BCCO). We perform transport measurements at ambient and high-pressure conditions up to  $\sim 55$  GPa, and magnetic susceptibility measurements for YCCO, LCCO, and BCCO. The Co and Cu  $K$ -edge and  $L$ -edge XAS, and Co  $2p$  XPS spectra are collected to study the valence state and the Co spin state. We present a computational simulation for the electronic structure using *ab initio* methods: DFT with local density approximation (LDA) method and LDA plus dynamical mean-field theory (DMFT) method. The energy levels of the Cu–O and Co–O bonding states are determined by a tight-binding modeling of the LDA bands. This also allows us to examine the crystal-field excitation energy in the  $ACu_3Co_4O_{12}$  system. The LDA + DMFT calculation exhibits the role of the electronic correlation. We calculate the spin-correlation function of the Cu using the LDA + DMFT method and discuss the Zhang-Rice singlet physics in YCCO.

This paper is organized as follows. In Sec. II, we summarize the experimental method including sample synthesis, and technical details of our computational simulations. In Sec. III A, the results of sample characterization, magnetic susceptibility, electrical resistivity, and x-ray absorption near-edge structure measurements at the Cu and Co  $K$  edges are shown. In Secs. III B and III C, we present LDA and LDA + DMFT calculations, and examine the electronic structure and the Zhang-Rice singlet physics in the studied compounds. In Sec. III D, we discuss Cu and Co  $L_{2,3}$ -edge XAS and Co  $2p$  XPS spectra. In Sec. III E, the pressure dependence of the electrical resistance is investigated. LDA +  $U$  calculations are performed to interpret the experimental result at elevated pressures. Finally, we summarize our results in Sec. IV.

## II. METHODS

### A. Experimental method

A precursor in synthesis of LCCO and BCCO samples was obtained using polymerized complex method [25].  $La(NO_3)_3 \cdot 6H_2O$  (99.9%) or  $Bi(NO_3)_3 \cdot 5H_2O$  (99.9%) was mixed with  $Cu(NO_3)_2 \cdot 3H_2O$  (99.9%) and  $Co(NO_3)_2 \cdot 6H_2O$  (99.9%) with a stoichiometric ratio of (La/Bi) : Cu : Co = 1 : 3 : 4 and then was dissolved in a nitric acid solution. A five-fold excess citric acid and a onefold excess of 1, 2-ethanediol was added to the solution, followed by heating to 423 K with stirring and maintained at this temperature for 30 min to dry. The dried powder was fired using a furnace at 673 K for 1 h, and at 973 K for 12 h in air with occasional grindings. The afforded precursor was mixed with an oxidizing agent  $KClO_4$  (99.9%) in mass ratio of 4 : 1 to compensate the oxygen content. The mixture was sealed off in a Pt capsule. The Pt capsule was placed into a (Mg, Co)O pressure-transmitting medium and compressed up to 12 GPa using a Walker-type high-pressure apparatus. The sample was subsequently heated to 1273 K in 15 min, maintained at this temperature for 30 min, and quenched to the room temperature. During the heat treatment, the applied pressure was retained. YCCO

sample was synthesized following Refs. [11,13]. Synchrotron x-ray powder diffraction (SXRD) data for LCCO and BCCO were collected using a Debye-Scherrer camera at the BL02B2 beam line of SPring-8 [26]. The powder sample was put into a Lindemann glass capillary tube with an inner diameter of 0.2 mm. The wavelength of 0.500 11 and 0.500 20 Å for LCCO and BCCO was used. Structure parameters were refined by the Rietveld method with the RIETAN-FP program [27]. X-ray absorption near-edge structure (XANES) spectra at Cu and Co  $K$  edges were collected at room temperature using the transmission method at the BL14B2 beam line in SPring-8.

Soft XAS data were collected at the Institute for Quantum Materials and Technologies (IQMT) beam line WERA at the KIT light source KARA (Karlsruhe, Germany). The photon energy resolution was set to 150, 300, and 350 meV at the O  $K$ , Co  $L_{2,3}$ , and Cu  $L_{2,3}$  edges, respectively. All spectra were measured with linearly polarized light, and the degree of linear polarization of the incident light was  $\sim 99\%$ . To reduce contribution of a surface contamination, the Co  $L_{2,3}$  and Cu  $L_{2,3}$  XAS were not only recorded in total-electron-yield (TEY) mode, but also in bulk-sensitive fluorescence-yield (FY) and inverse partial-fluorescence yield (IPFY) mode simultaneously. The O  $K$  XAS was collected in FY mode. FY and IPFY are both bulk sensitive, yet “direct” FY usually suffers from the strong self-absorption and saturation effects [28], especially at the intense “white line” of transition-metal  $L$  edges. The weak self-absorption of the O  $K$  is corrected [29]. However, for the Co  $L_{2,3}$  and Cu  $L_{2,3}$  edges, these self-absorption and saturation effects may change spectral shapes and energy positions significantly. The correction at the Co and Cu  $L$  edges, hence, is less reliable. In order to record the correct Co and Cu XAS we have therefore applied IPFY which is intrinsically free from self-absorption and saturation distortions. An energy-resolving four-element silicon drift detector (SDD) was used for collecting the FY and IPFY data [30,31]. The angle between the incident light and the SDD was set as  $30^\circ$ . Single-crystal NiO was also measured before and after each measurement to serve as an energy reference for calibrating the incident photon energy at all edges, with accuracy better than 30 meV for all XAS measurements.

The Co  $2p$  XPS was carried out at the ASPHERE III end station at the Variable Polarization XUV Beam line P04 of the PETRA III storage ring at DESY (Hamburg, Germany). All XPS data were collected at a sample temperature of 300 K and in ultrahigh vacuum  $< 3 \times 10^{-10}$  mbar. The incident photon energy was set to 2 keV, and the overall energy resolution was set to  $\sim 300$  meV.

Magnetization measurements were conducted using a superconducting quantum interference device (SQUID, Quantum Design MPMS3) between 5 and 300 K under external magnetic fields up to 50 kOe. Electrical resistance under ambient pressure was measured using the physical property measurement system (PPMS, Quantum Design) between 5 and 300 K with the dc four-terminal method. Dense pellets of LCCO and BCCO were prepared by compressing the powder sample using the Walker-type high-pressure apparatus. High-pressure electrical resistance data were obtained between 10 and 300 K up to a pressure of  $\sim 55$  GPa using a diamond anvil cell. The electrical resistance of each sample was measured using the ac four-probe method between 8 and 300 K, up to a

maximum pressure of  $\sim 55$  GPa. Prior to the measurements, a fine anhydrite powder was pressed onto the gasket surface to provide electrical insulation, and both the sample powder and the Pt electrodes were placed on this insulation. The applied pressure was determined by fluorescence manometry using ruby chips positioned around the sample. In the electrical resistance measurements, the initial cross-sectional area of the specimen was approximately  $40 \mu\text{m} \times 30 \mu\text{m}$ , and the distance between the probes was approximately  $30 \mu\text{m}$ .

## B. Computational details

We perform DFT calculations for the experimental crystal structure at ambient pressure of the studied compounds using the WIEN2K package [32] within the LDA for the exchange-correlation potential. For a comparison, we calculate the LDA bands of a canonical perovskite cobaltite  $\text{LaCoO}_3$  with a low-temperature experimental lattice parameter ( $T_{\text{lattice}} = 5$  K) [33]. To include the electronic correlation effects, we perform LDA + DMFT calculations [34–36], where the Cu  $3d$ , Co  $3d$ , and O  $2p$  bands in the LDA results are mapped onto a tight-binding lattice model using the WANNIER90 and WIEN2WANNIER packages [37,38]. Then, the tight-binding model is augmented by the onsite interactions on the Cu and Co  $3d$  shells with Hubbard  $U$  and Hund’s  $J$  parameters are (8.5 eV, 0.98 eV) for the Cu and (6.0 eV, 0.8 eV) for Co site [7,33]. The continuous-time quantum Monte Carlo (CT-QMC) method with the hybridization expansion formalism [39–41] is used to solve the auxiliary Anderson impurity model (AIM) in the DMFT self-consistent calculation. Only density-density terms in the onsite interaction are taken into account in the CT-QMC calculations for computational efficiency. This approximation is valid for the Cu impurity with only single  $xy$  orbital active. It also represents the atomic multiplet of the Co site reasonably well and was used to study the Co spin states in perovskite cobaltites [33]. We follow Refs. [42,43] for determining the double-counting correction on the Cu and Co  $3d$  orbitals. The valence density of states on the real frequency axis are obtained with the local self-energies analytically continued to the real-frequency axis using maximum entropy method [44,45]. The LDA + DMFT calculations are performed at  $T = 300$  K. Weights of the Cu atomic states given as the partial traces of the reduced density matrix and the imaginary-time local spin-spin correlation function  $\chi_{\text{spin}}(\tau) = \langle S_z(\tau)S_z(0) \rangle$  are measured directly in the CT-QMC simulation for the AIM of the Cu site [39,46,47]. To find equilibrium atomic positions at reduced lattice parameters to examine the electronic structure change at elevated pressures, we use a computationally cheap LDA +  $U$  scheme implemented in the WIEN2K package [32]. In the LDA +  $U$  calculations, effective  $U$  values ( $U_{\text{eff}} = U - J$ ) are set to  $U_{\text{eff}} = 2.0$  and  $7.0$  eV for Co and Cu sites, respectively.

To simulate Co  $L_{2,3}$ -edge XAS and  $2p$  XPS, we calculate the core-level spectral intensities within the LDA + DMFT scheme. This consists in postprocessing of the LDA + DMFT calculations for the valence electrons described above, where the AIM with the LDA + DMFT hybridization densities  $\Delta(\omega)$  is extended to include explicitly the Co  $2p$  core orbitals and Co  $2p$ - $3d$  core-valence Coulomb multiplet interaction. Our computational details for calculating the core-level spectral

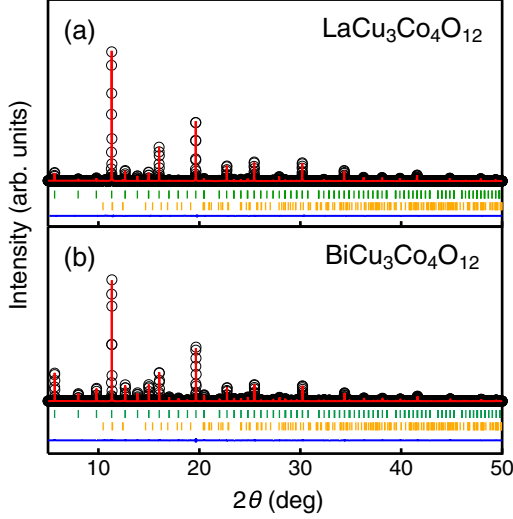


FIG. 2. Observed SXRD patterns and Rietveld refinement results for (a)  $\text{LaCu}_3\text{Co}_4\text{O}_{12}$  (LCCO) and (b)  $\text{BiCu}_3\text{Co}_4\text{O}_{12}$  (BCCO). The circles (black) and solid lines (red) are observed and calculated patterns, respectively. The difference of the observed and calculated patterns is shown at the bottom (blue). The vertical marks (green: ACCO, orange: CuO) indicate the Bragg reflection positions.

intensities of the LDA + DMFT AIM using a configuration-interaction impurity solver can be found in Refs. [48–50]. We also calculate the Co  $L_{2,3}$  XAS spectra using a conventional  $\text{CoO}_6$  cluster model which implements the same Co intra-atomic Hamiltonian with the LDA + DMFT AIM, while the continuous DMFT hybridization densities  $\Delta(\omega)$  are replaced by discrete levels composed of the nearest-neighboring ligand  $2p$  orbitals. Thus, differences in the simulated spectra of the LDA + DMFT AIM and the  $\text{CoO}_6$  cluster can be attributed to long-distance hybridization effects beyond the single  $\text{CoO}_6$  unit [51].

### III. RESULTS AND DISCUSSION

#### A. Structural characterization, magnetic susceptibility, electrical resistivity, and XANES measurements

Almost single-phase samples of LCCO and BCCO were synthesized in the high-pressure and high-temperature conditions. Figure 2 shows the SXRD pattern and the Rietveld refinement result. The cubic  $A$ -site ordered perovskite structure (space group:  $Im\bar{3}$ , Fig. 1) was used to fit the Bragg reflections of the primary phase, though the impurity phase of CuO ( $< 5.0$  wt.%) was also detected. The structure parameters obtained from the final Rietveld refinement are listed in Table I, giving a reliable result with small reliability factors  $R$  and goodness-of-fit indicator  $S$ . The lattice constant, M–O bond lengths, and bond valence sums (BVSs) for YCCO, LCCO, and BCCO are also summarized in Table I. The increase from  $A = \text{Y}$  to La or Bi of the lattice constant and the M–O bond length is consistent with the extension of the  $A$ -site ions; Shannon effective ionic radii are 1.019, 1.16, and 1.17 Å for  $\text{Y}^{3+}$ ,  $\text{La}^{3+}$ , and  $\text{Bi}^{3+}$  in the eight coordination [55]. The BVSs for the Cu and Co ions are almost identical in the studied compounds.

TABLE I. Structure parameters for  $\text{ACu}_3\text{Co}_4\text{O}_{12}$  at room temperature from the Rietveld refinement. The space group is  $Im\bar{3}$  (No. 204) for all compounds with atomic sites:  $A$   $2a$  (0,0,0), Cu  $6b$  (1/2, 1/2, 0), Co  $8c$  (1/4, 1/4, 1/4), O  $24g$  ( $x, y, 0$ ), and with lattice constant  $a$ . The BVSs were calculated using the following parameters:  $b_0 = 0.37\text{Å}$  for all atoms,  $r_0 = 2.019\text{Å}$  for  $\text{Y}^{3+}$ ,  $r_0 = 2.172\text{Å}$  for  $\text{La}^{3+}$ ,  $r_0 = 2.094\text{Å}$  for  $\text{Bi}^{3+}$ ,  $r_0 = 1.735\text{Å}$  for  $\text{Cu}^{3+}$ , and  $r_0 = 1.637\text{Å}$  for  $\text{Co}^{3+}$  [52–54]. The occupancy factors for all atoms were fixed to the unity. These structure parameters are used as input for the DFT calculations.

	$A = \text{Y}$	$A = \text{La}$	$A = \text{Bi}$
$a$ (Å)	7.12393(2)	7.18716(4)	7.18332(3)
$x$	0.3041(2)	0.3115(3)	0.3089(2)
$y$	0.1726(2)	0.1780(3)	0.1777(3)
$U_{\text{iso}}(A) \times 10^3$ (Å <sup>2</sup> )	2.0(1)	1.7(1)	6.8(1)
$U_{\text{iso}}(\text{Cu}) \times 10^3$ (Å <sup>2</sup> )	2.3(1)	3.4(1)	2.4(1)
$U_{\text{iso}}(\text{Co}) \times 10^3$ (Å <sup>2</sup> )	0.7(1)	1.5(1)	2.6(1)
$U_{\text{iso}}(\text{O}) \times 10^3$ (Å <sup>2</sup> )	3.4(3)	4.5(4)	7.9(5)
A–O ( $\times 12$ ) (Å)	2.4910(13)	2.578(3)	2.5599(17)
Cu–O ( $\times 4$ ) (Å)	1.8601(12)	1.8632(19)	1.8741(17)
Cu–O ( $\times 4$ ) (Å)	2.7180(14)	2.682(3)	2.6918(18)
Co–O ( $\times 6$ ) (Å)	1.9037(4)	1.9214(7)	1.9168(6)
BVS[A]	3.35	4.05	3.41
BVS[Cu]	3.13	3.05	3.05
BVS[Co]	2.92	2.81	2.82
$R_{\text{wp}}$ (%)	3.29	7.13	6.11
$R_{\text{B}}$ (%)	3.35	4.17	2.43
$S$	1.092	1.045	1.021

Figure 3(a) shows the temperature dependence of the electrical resistivity. Although the absolute values cannot be compared between the polycrystalline pellet samples, the resistivity of all three compounds displayed an insulating behavior, exhibiting a decrease in  $\rho$  with the temperature increased. The insulating behavior is consistent with previous reports for YCCO [11]. Figure 3(b) shows a fitting result of the electric conductivity ( $\sigma$ ) using the Arrhenius equation  $\ln \sigma = -(E_a/k_B T) + C$ , where  $E_a$ ,  $k_B$ ,  $T$ ,  $C$  denote the activation energy, Boltzmann constant, temperature, and a constant term, respectively. The activation energy  $E_a$  extracted in the high-temperature region (orange) shows a systematic increase for the smaller ionic radii as 51 meV in BCCO, 123 meV in LCCO, and 344 meV in YCCO. The  $E_a$  extracted in the low-temperature region (blue) is 25.8 meV in BCCO, 39.5 meV in LCCO, and 68.1 meV in YCCO. Thus, the trend of  $E_a$  is the same as that in the high-temperature region.

Figure 4 shows the field-cooling (FC) magnetic susceptibilities of LCCO and BCCO. A 1-kOe external field was applied in the measurement. The zero-field-cooling measurements (not shown) give a nice agreement with the FC data. No signature of a magnetic transition is detected in the studied temperatures. The susceptibilities contain a Curie-Weiss-type (CW) response due to magnetic impurities admixed in the high-pressure synthesis. A CW fitting for the magnetic susceptibility was performed as  $\chi = C_{\text{CW}}/(T - \theta_{\text{W}}) + \chi_0$  (see Fig. 4), where  $C_{\text{CW}}$  is a Curie constant,  $\theta_{\text{W}}$  is the Weiss temperature,  $\chi_0$  is a constant term independent of the temperature, which gives  $C_{\text{CW}}$  of 0.687 and 0.452 emu K/mol for LCCO

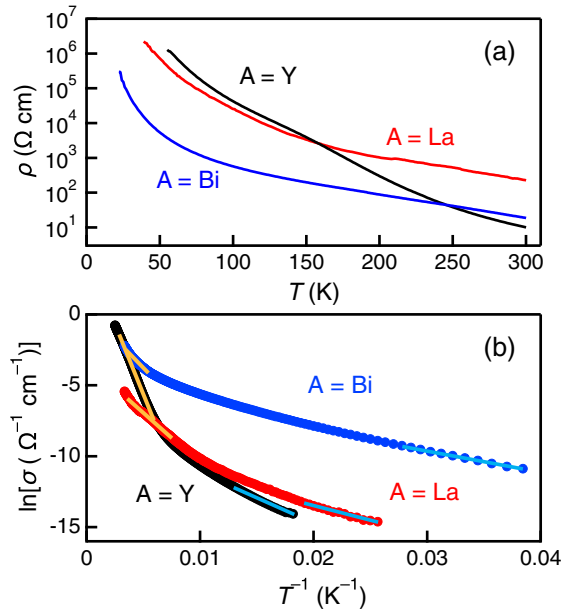


FIG. 3. (a) Temperature dependence of the electrical resistivity  $\rho$  and (b) the electrical conductivity in a logarithm scale ( $\ln\sigma$ ) for inverse temperature ( $T^{-1}$ ) for  $\text{YCu}_3\text{Co}_4\text{O}_{12}$  (black),  $\text{LaCu}_3\text{Co}_4\text{O}_{12}$  (red), and  $\text{BiCu}_3\text{Co}_4\text{O}_{12}$  (blue).

and BCCO, respectively, in proximity to 0.560 emu K/mol for YCCO [11]. The Weiss temperature  $\theta_W$  is estimated as  $-125.42$ ,  $-24.54$ , and  $-26.85$  K for YCCO, LCCO, and BCCO, respectively, indicating antiferromagnetic impurities are present in the ACCO samples. The inset of Fig. 4 shows

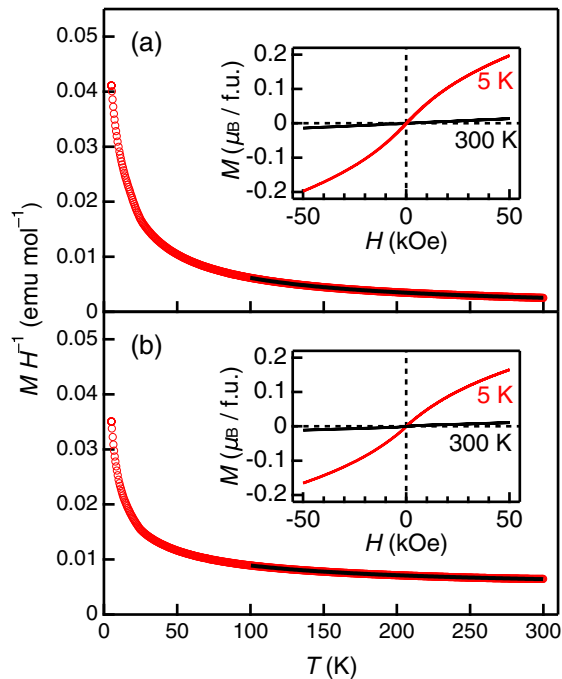


FIG. 4. Temperature dependence of the magnetic susceptibility for (a)  $\text{LaCu}_3\text{Co}_4\text{O}_{12}$  and (b)  $\text{BiCu}_3\text{Co}_4\text{O}_{12}$  measured in an external field of 1 kOe on FC. The black line (100–300 K) represents the fitting result using the Curie-Weiss law. The inset shows isothermal magnetization curves at 5 K and 300 K.

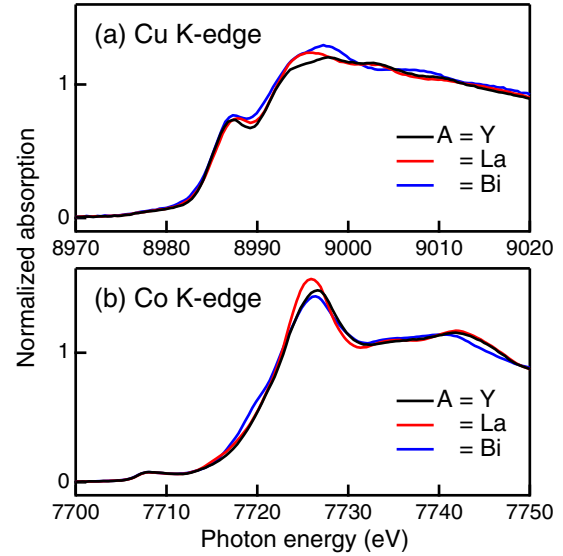


FIG. 5. XANES spectra of (a) Cu  $K$  edge and (b) Co  $K$  edge for  $\text{ACu}_3\text{Co}_4\text{O}_{12}$ . The spectra are measured at room temperature.

the isothermal magnetization ( $M$ – $H$ ) curves at 5 and 300 K for LCCO and BCCO. Both exhibited no spontaneous magnetization at 5 K, excluding the possibility of a ferromagnetic transition. This is similar to the magnetic property of YCCO.

Figure 5 summarizes the XANES spectra of the studied compounds. In the previous study [13], the XANES spectra of YCCO were compared with those of reference Co and Cu compounds, and the valence state is proposed as  $\text{YCu}_3^{3+}\text{Co}_4^{3+}\text{O}_{12}$ . LCCO and BCCO show similar absorption energies both at the Co and Cu  $K$  edges with YCCO, suggesting the valence state of  $\text{LaCu}_3^{\sim 3+}\text{Co}_4^{\sim 3+}\text{O}_{12}$  and  $\text{BiCu}_3^{\sim 3+}\text{Co}_4^{\sim 3+}\text{O}_{12}$ .

## B. LDA and LDA + DMFT simulation for the electronic structure

The experimental results above suggest the valence model of  $\text{A}^{3+}\text{Cu}_3^{\sim 3+}\text{Co}_4^{\sim 3+}\text{O}_{12}^{2-}$  for the studied compounds at ambient pressure. No clear signature of a spin-state transition of the Co ion or insulator-to-metal transition was observed. To find the energetics of the Cu–Co–O system (covalent bonding, crystal field, and electronic correlation), we first calculate the electronic structure of YCCO as a representative of  $\text{ACu}_3\text{Co}_4\text{O}_{12}$  using two *ab initio* methods, LDA and LDA + DMFT. The former represents noninteracting bands and is used to study the crystal-field  $d$ -orbital energies, and Cu–O and Co–O bonding properties. The DMFT provides dynamical correlation effects within the Co 3d and Cu 3d shells to the noninteracting LDA bands.

Figure 6(c) shows LDA density of states resolved for the Co 3d, Cu 3d, and O 2p orbitals. The Co 3d ( $e_g$ ,  $t_{2g}$ ) and Cu  $xy$  states are positioned near the Fermi energy  $E_F$ . The Co  $t_{2g}$  states split into a singlet ( $a_{1g}$ ) and a doublet ( $e_{g\pi}$ ) due to a trigonal distortion of the  $\text{CoO}_6$  octahedra. We average the  $a_{1g}$  and  $e_{g\pi}$  states in the spectra and results below for simplicity of the presentation. To study the Cu–O and Co–O bondings, Figs. 6(a) and 6(b) present the spectra calculated for the  $\text{Cu}_3\text{O}_{12}$  and  $\text{Co}_4\text{O}_{12}$  sublattices separately. The former

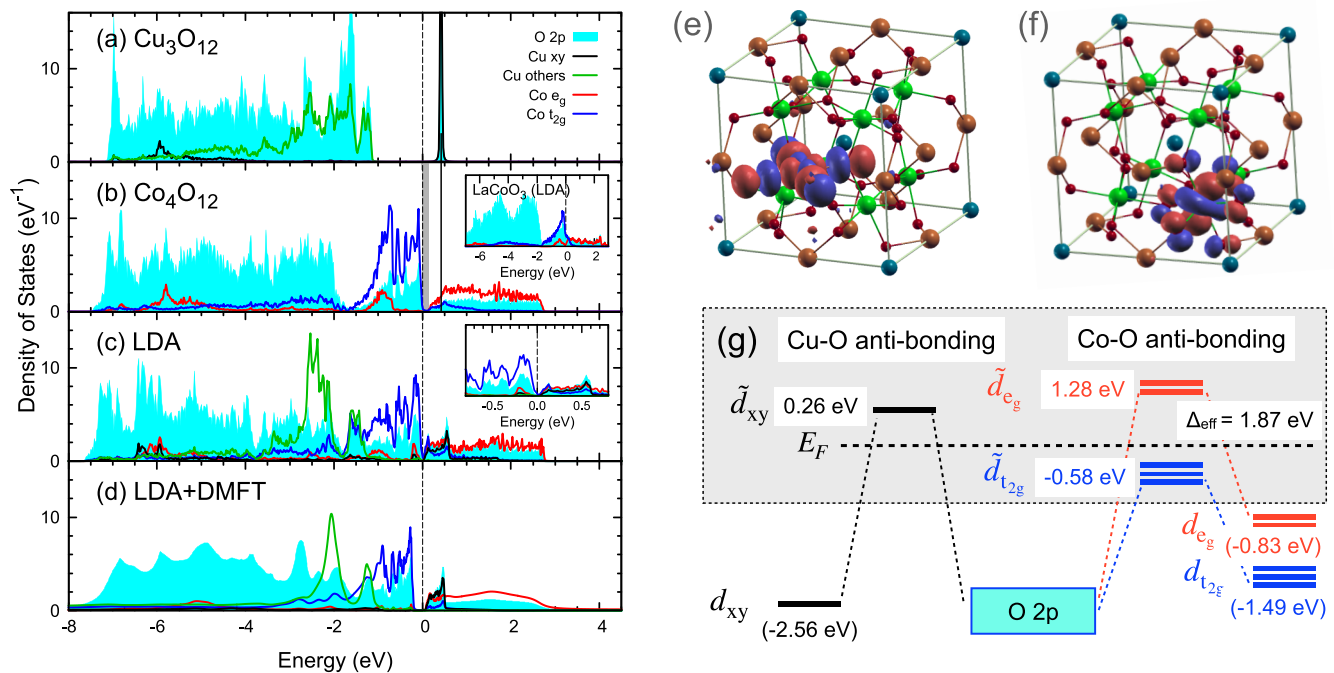


FIG. 6. The LDA density of states for (a)  $\text{Cu}_3\text{O}_{12}$  (no Co) sublattice and (b)  $\text{Co}_4\text{O}_{12}$  (no Cu) sublattice in YCCO, and (c) YCCO. The inset of (b) shows the LDA density of states for  $\text{LaCoO}_3$  as a reference of perovskite cobaltite. The low-energy region of the LDA spectra is zoomed in the inset of (c). (d) LDA + DMFT density of states for YCCO. The Wannier functions for the antibonding state of (e) Cu  $xy$  and (f) a Co  $t_{2g}$  states. (g) Sketch of the energy diagram for the relevant  $d$  states. The hybridization of atomic Co  $d_{e_g}$ ,  $d_{t_{2g}}$  and Cu  $d_{xy}$  orbitals with the O  $2p$  orbitals lead the antibonding Cu  $\tilde{d}_{xy}$  and Co  $\tilde{d}_{e_g}$ ,  $\tilde{d}_{t_{2g}}$  states. The energies of the atomic orbitals are taken from the diagonal elements in the tight-binding Hamiltonian constructed from the LDA bands (spanning the Co  $d$ , Cu  $d$ , and O  $2p$  bands). The energy levels of the antibonding Cu  $\tilde{d}_{xy}$  and Co  $\tilde{d}_{e_g}$ ,  $\tilde{d}_{t_{2g}}$  states are computed by the same procedure but for a tight-binding model obtained by projecting low-energy antibonding states (of Cu  $xy$  and Co  $3d$  orbital symmetries).

(latter) is obtained by eliminating the Co (Cu) orbitals in the tight-binding Hamiltonian constructed from the LDA bands. A formation of the Cu–O and Co–O bonding and antibonding states is illustrated in Fig. 6(g). In the  $\text{Cu}_3\text{O}_{12}$  sublattice [see Fig. 6(a)], the Cu  $xy$  state pointing to the nearest-neighboring ligands strongly hybridizes with the O  $2p$  states via the  $\sigma$ -type bonding, resulting in the well-split bonding ( $\sim -6$  eV) and antibonding ( $\sim 0.3$  eV) states. The antibonding Cu  $xy$ -O  $2p_\sigma$  state has large weight on the four O atoms [see the Wannier function in Fig. 6(e)]. The antibonding state shows a sharp peak in Fig. 6(a) since each  $\text{CuO}_4$  plaquette is orthogonal and isolated to each other in the crystal structure, Fig. 1. Due to the strong Cu  $xy$ -O  $2p_\sigma$  hybridization and a large tilt of  $\text{CoO}_6$  octahedra, the other Cu  $3d$  orbitals ( $z^2$ ,  $x^2 - y^2$ ,  $zx$ ,  $yz$ ) are positioned well below the Fermi energy. The orbital-resolved spectra for the Cu orbitals are found in the Supplemental Material [56].

In the  $\text{Co}_4\text{O}_{12}$  sublattice, we find a small gap ( $\sim 0.15$  eV) between the Co  $t_{2g}$  and  $e_g$  states, as highlighted by a gray shadow in Fig. 6(b). Here, we refer to noninteresting LDA bands of canonical perovskite  $\text{LaCoO}_3$  [see inset of Fig. 6(b) and Ref. [33]], showing a metallic behavior with overlapping Co  $e_g$  and  $t_{2g}$  bands. The effective crystal-field splitting  $\Delta_{\text{eff}}$  defined as the splitting of the Co  $e_g$  and  $t_{2g}$  antibonding orbitals is estimated to 1.87 eV in YCCO [see Fig 6(g)], while  $\Delta_{\text{eff}}$  is 1.6 eV in  $\text{LaCoO}_3$ . The  $\Delta_{\text{eff}}$  value is 1.81 and 1.83 eV for LCCO and BCCO, respectively.  $\text{LaCoO}_3$  displays a spin-state transition near 100 K from the low-spin ( $S = 0$ )

with fully filled  $t_{2g}$  orbitals, to magnetic high-spin ( $S = 2$ ) or intermediate-spin ( $S = 1$ ) states with excitations from the Co  $t_{2g}$  to  $e_g$  orbitals [15,18,57–62]. The  $\Delta_{\text{eff}}$  estimates indicate that the low-spin state, preferred for large  $\Delta_{\text{eff}}$ , is more stable in YCCO, LCCO, and BCCO than  $\text{LaCoO}_3$ .

In combining the Cu–O and Co–O network discussed above, the low-energy excitation of YCCO builds on the Cu  $xy$  antibonding state embedded into the ionic crystal-field gap between the Co  $e_g$  and  $t_{2g}$  states [Figs 6(g) and 6(a)–6(c)]. This, however, does not yield a metallic state. The LDA result in Fig. 6(c) presents a small hybridization gap ( $E_{\text{gap}} \sim 0.05$  eV). The Cu  $xy$  antibonding state hybridizes dominantly with the Co  $t_{2g}$  states via a  $\pi$ -like coupling, resulting in the gap. The hybridization can be inferred from the shape of the tails of their Wannier functions in Figs. 6(e) and 6(f). The hybridization gap in the noninteracting bands is not opening in LCCO and BCCO (not shown) due to a larger volume which reduces the hybridization of the Cu  $xy$  and Co  $t_{2g}$  orbitals.

Figure 6(d) shows the LDA + DMFT density of states for YCCO. Overall electronic structure does not change from the LDA result in Fig. 6(c). A main consequence of the electronic correlation is an increase of the charge gap with an upward shift of the unoccupied Cu  $xy$  and Co  $e_g$  bands. The nonmagnetic insulating state with a small charge gap is consistent with the experimental observations in Sec. III A. We also calculated the valence spectra for LCCO and BCCO by the LDA + DMFT method, Fig. 7. The charge gap of LCCO is smaller than that of YCCO. BCCO exhibits a pseudo-gap-like

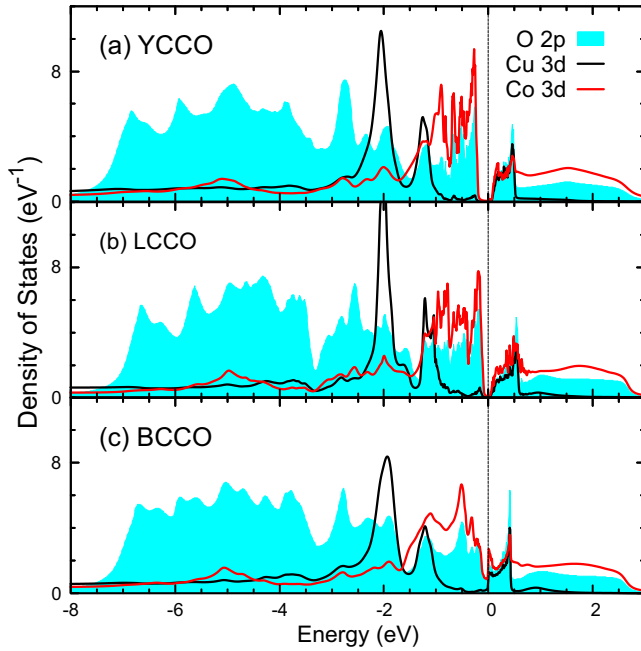


FIG. 7. The LDA + DMFT density of states for (a) YCCO, (b) LCCO, and (c) BCCO.

feature near the Fermi energy. The *A*-site element dependence of the low-energy structure agrees with the experimental trend of the activation energy in Sec. III A.

The electronic structure obtained above sheds a light on the valence change by electron and hole doping in the  $ACu_3Co_4O_{12}$  family, mentioned in Sec. I. The top of the valence band in YCCO has a Co  $t_{2g}$  character, while the bottom of the conduction band is composed of the Cu  $xy$  state with which broad Co  $e_g$  band is overlapped [see Figs. 6(c) and 6(d)]. This serves as a qualitative explanation for the experimental observation; the electron (hole) doping changes the Cu (Co) valence dominantly. As a validity of this simple rigid-band picture, we perform a supplemental LDA + DMFT calculation for electron- and hole-doped YCCO (see Fig. 8). The asymmetry in the element character of the doped carriers is seen in the calculated results: Doped holes reside on the Co sites, while doped electrons go into both the Cu and Co sites. As expected for the oxides with high-valence Cu and Co ions, the carriers are also doped into the O sites. A quantitative evaluation for a specific 2+ or 4+ *A* site requires a lattice parameter relaxation which would renormalize the Co and Cu bandwidths to some extent, though it is beyond the scope of this study. In the studied hole concentration, i.e., up to 1 hole per formula unit, mimicking  $A^{2+}Cu_3Co_4O_{12}$  case, the Co spin-state transition from the low-spin ground state does not occur, which is consistent with the stable Co low-spin state in  $CaCu_3Co_4O_{12}$  [12].

### C. Cu spin dynamics in YCCO

Next we investigate the charge and spin dynamics on the Cu site. Figure 9(b) shows (projected) atomic weights on the Cu site in the LDA + DMFT result for YCCO. We find the highest atomic weight in the  $N = 9$  charge sector and some

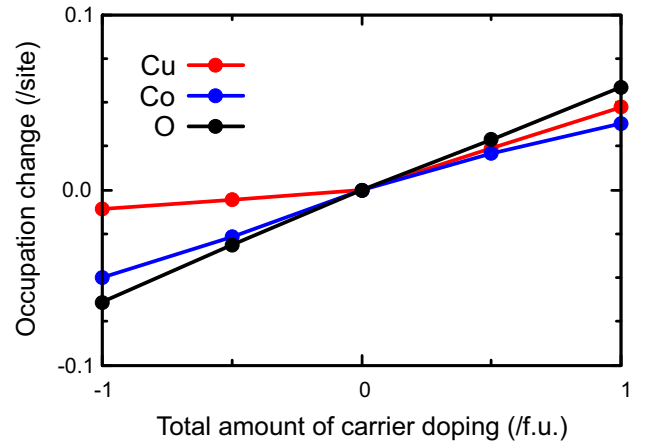


FIG. 8. The change of the electron occupation (per site) on the Cu, Co, and O sites from the stoichiometric YCCO by the electron or hole doping. Here the LDA + DMFT method was employed and YCCO structure in Table I was used. The plus (minus) sign indicates the electron (hole) doping to the stoichiometric filling of YCCO.

distributions to the  $N = 8$  and 10 sectors. The calculated total Cu 3*d* occupation is  $\langle N_d \rangle = 8.9$ . This Cu occupation is not contradictory to the valence model of  $A^{3+}Cu_3^{3+}Co_4^{3+}O_{12}^{2-}$  since this valence model represents the electron distributions among the Cu and Co low-energy antibonding states.

Figure 9(a) shows the spin-correlation function  $\chi_{\text{spin}}(\tau)$  calculated at the Cu site. A large instantaneous response

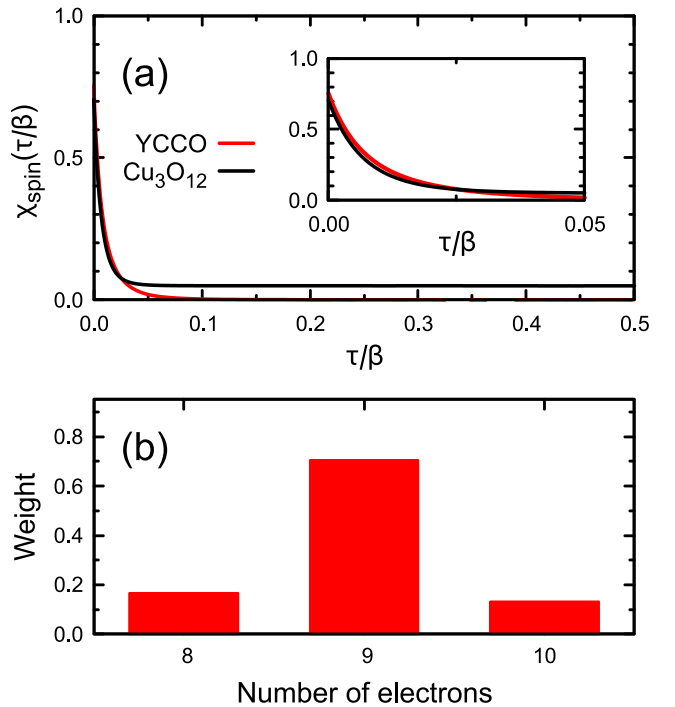


FIG. 9. (a) The spin-correlation function  $\chi_{\text{spin}}(\tau)$  calculated at the Cu site in YCCO (red) using the LDA + DMFT method along the imaginary-time axis. Here,  $\beta$  is the inverse temperature corresponding to the simulation temperature ( $T = 300$  K). The  $\chi_{\text{spin}}(\tau)$  calculated for the  $Cu_3O_{12}$  sublattice in YCCO is shown for comparison (black). (b) Weights of the atomic states at the Cu site.

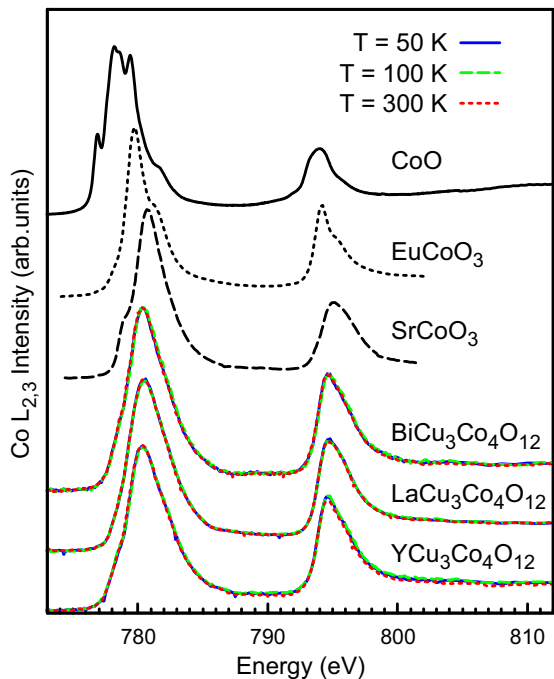


FIG. 10. Co  $L_{2,3}$  XAS spectra of the studied compounds. The spectra are measured using IPFY mode at 50 K (blue), 100 K (green), and 300 K (red).  $\text{EuCoO}_3$  ( $\text{Co}^{3+}$  low-spin reference) [12],  $\text{SrCoO}_3$  ( $\text{Co}^{4+}$  reference) [12], and  $\text{CoO}$  ( $\text{Co}^{2+}$  reference) [12] spectra are shown together.

$[\chi_{\text{spin}}(\tau = 0^+) \sim 0.7]$  is found. This is an expected behavior for the dominant  $d^9$  local configuration [Fig. 9(b)] with the spin  $S = \frac{1}{2}$ . However, the instantaneous spin response is screened in time rapidly by a coupling with the bath composed of the valence electrons. Thus, the Cu spin does not lead to a local-moment behavior in the magnetic susceptibility. To figure out the underlying mechanism of the Cu spin screening, in Fig. 9(a) (red curve), we calculate the  $\chi_{\text{spin}}(\tau)$  for the  $\text{Cu}_3\text{O}_{12}$  model introduced in Fig. 6(a), where the hybridization with the Co  $3d$  states is absent. This partial model result resembles that of the full model of YCCO well, especially in a short-time response [see the inset of Fig. 9(a)], indicating that the spin screening occurs dominantly with nearest-neighboring ligands. This behavior fits with the picture of the Zhang-Rice singlet state where a spin-singlet state is formed between the Cu  $xy$  and ligand  $2p$  holes locally on the  $\text{CuO}_4$  plaquette [23,24]. However, we find that  $\chi_{\text{spin}}(\tau)$  of the  $\text{Cu}_3\text{O}_{12}$  model does not decay to zero and it leaves a residual long-time response of  $\chi_{\text{spin}}(\tau = \beta/2) \sim 0.05$ . Thus, the hybridization with the Co  $3d$  states also affects the Cu spin dynamics, and is important for fully quenching the Cu spin in YCCO.

#### D. $2p$ core-level XAS and XPS spectra

Figure 10 shows the Co  $L$ -edge XAS spectra for all samples together with the reference spectra of  $\text{CuO}$  ( $\text{Cu}^{2+}$ ),  $\text{SrCoO}_3$  ( $\text{Co}^{4+}$ ) [12],  $\text{EuCoO}_3$  ( $\text{Co}^{3+}$ ) [12], and  $\text{CoO}$  ( $\text{Co}^{2+}$ ). The Co  $L_{2,3}$  XAS is sensitive to the Co spin state as well as the Co valence state [61]. The Co  $L_{2,3}$  XAS spectra of the studied compounds are similar with that of  $\text{EuCoO}_3$ , a

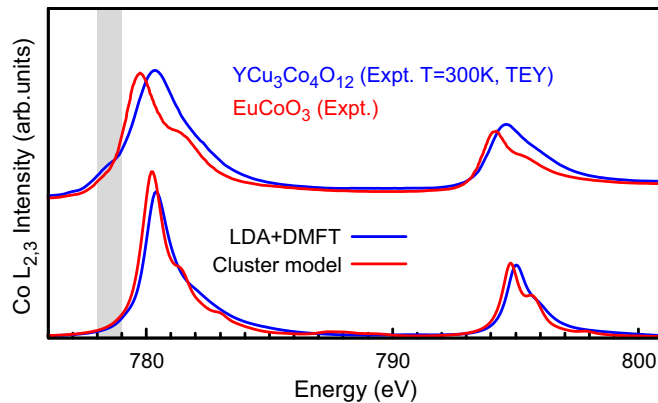


FIG. 11. Co  $L_{2,3}$  XAS spectra calculated by the  $\text{CoO}_6$  cluster model (bottom, red) and the LDA + DMFT AIM (bottom, blue). The experimental spectra of YCCO measured with the TEY mode and  $\text{EuCoO}_3$  [12] are shown together.

reference of the low-spin  $\text{Co}^{3+}$  system, but the line shape as well as the absorption energies differ from  $\text{SrCoO}_3$  ( $\text{Co}^{4+}$ ) and  $\text{CoO}$  ( $\text{Co}^{2+}$ ). Similar to previous Co  $L_{2,3}$  XAS studies [12] for YCCO and  $\text{CaCu}_3\text{Co}_4\text{O}_{12}$  using the TEY method, however, the Co  $L_{2,3}$  XAS spectra in all studied  $\text{ACu}_3\text{Co}_4\text{O}_{12}$  are rather broad compared with the spectrum of  $\text{EuCoO}_3$ . To elaborate this observation, we simulate the XAS spectra by the LDA + DMFT AIM and cluster model, Fig. 11. Here, we show the Co XAS of YCCO measured in TEY mode to directly compare with the reference spectrum of  $\text{EuCoO}_3$ . The LDA + DMFT AIM considers the hybridization of the Co orbitals with the long-distant ions including the Cu  $3d$  ones [48]. On the other hand, the  $\text{CoO}_6$  cluster model describes the hybridization only with the nearest-neighboring ligands. The cluster-model result for YCCO is similar with the spectrum of  $\text{EuCoO}_3$ , exhibiting a shoulder feature around 781.5 eV in the Co  $L_3$  main line which is a well-known characteristic for ionic low-spin Co system [61]. Thus, the broad main-line feature is not intra-atomic or hybridization with the ligands origin. Although the ground state is the low-spin singlet in the LDA + DMFT AIM, the LDA + DMFT XAS spectrum is broader substantially than the  $\text{CoO}_6$  cluster-model one, accompanied by a continuumlike tail in the high-energy side, and reproduces the experimental line shape well. The results of the two theoretical methods suggest that (1) the Co ion has the trivalent low-spin state, and (2) the broad Co  $L_{2,3}$  XAS spectrum is intrinsic in YCCO that is related with the hybridization effect with the Cu ions. In the experimental data, a small intensity is found in the pre-edge region ( $\sim 778$  eV), indicated by a gray shadow in Fig. 11, which is probably attributed to  $\text{Co}^{2+}$  impurities.

To further support the trivalent low-spin Co state, Fig. 12 shows the Co  $2p_{3/2}$  XPS spectra for three compounds. The spectrum simulated by the LDA + DMFT AIM for YCCO is also shown. Our experimental XPS result for YCCO agrees well with previous studies by Mizokawa *et al.* [23] who pointed out that the binding energy  $E_B$  of the Co  $2p_{3/2}$  satellite feature in YCCO matches well with that of  $\text{LaCoO}_3$ , while that of  $\text{SrCoO}_3$  is about 1–2 eV lower, as indicated by arrows in Fig. 12. The Co  $2p_{3/2}$  satellite binding energy is sensitive to the valence state and spin state of the Co ion [65,66].

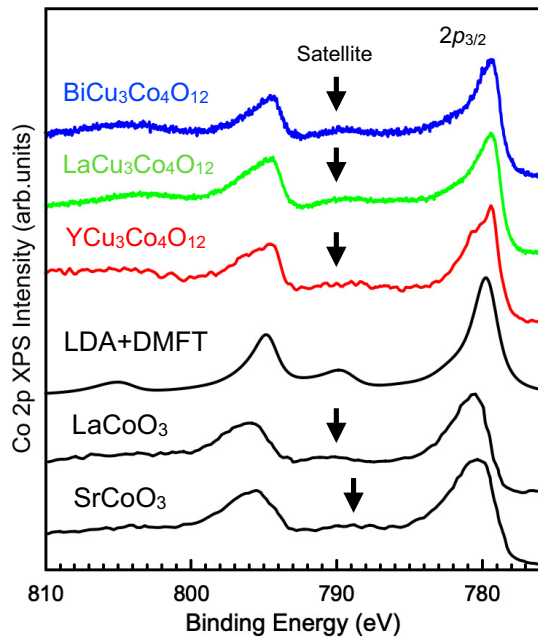


FIG. 12. Co 2p XPS spectra of YCCO (red), LCCO (green), BCCO (blue), and the LDA + DMFT AIM result for YCCO (black). The Co 2p XPS spectra of the reference compounds: LaCoO<sub>3</sub> (green) and SrCoO<sub>3</sub> (pink) taken from Ref. [63] are also shown for comparison. The Co 2p<sub>3/2</sub> satellite feature is indicated by an arrow.

The LDA + DMFT AIM reproduces the satellite position in the experimental data nicely.

In Fig. 10, the temperature dependence of the Co L<sub>2,3</sub> XAS spectra is negligibly weak in YCCO, LCCO, and BCCO. This indicates that the spin-state transition does not occur in the studied temperature range.

We next discuss the Cu L<sub>3</sub> XAS. Figure 13 displays the Cu L<sub>3</sub> spectra of studied samples and of the reference NaCuO<sub>2</sub> (Cu<sup>3+</sup>) [12]. All compounds show a prominent peak at about 933 eV. The absorption energy of this peak is very similar with that in the Cu<sup>3+</sup> reference oxide, NaCuO<sub>2</sub>. The Cu<sup>2+</sup> absorption feature is found around 931 eV, while its intensity is rather weak compared to the Cu<sup>3+</sup> feature, indicating that the Cu valence is close to trivalent. In order to quantitatively determine the Cu valence, we have performed a fitting analysis for all Cu L<sub>3</sub>-XAS spectra. We obtained estimates of the Cu valence as +2.91, +2.93, and +2.83 for YCCO, LCCO, and BCCO, respectively. Our fitting analysis can be found in the Supplemental Material [56].

We comment on the Zhang-Rice singlet state from the XAS point of view. As pointed out in Ref. [24] for CaCu<sub>3</sub>Co<sub>4</sub>O<sub>12</sub> and doped cuprates, the high-energy absorption feature (~933 eV), referred to as the Cu<sup>3+</sup> peak above, corresponds to the transition from  $|d^9\bar{L}\rangle \rightarrow |\underline{c}d^{10}\bar{L}\rangle$ , where  $d$  and  $\underline{c}$  denote an electron on the Cu 3d shell and a hole on the Cu 2p core level, respectively. On the other hand, the weak broad feature around 942 eV is attributed to the  $|d^8\rangle \rightarrow |\underline{c}d^9\rangle$  excitation. These two transitions are possible for the formally trivalent Cu. The former is a known signature of the Zhang-Rice singlet ground state. The Cu<sup>2+</sup> feature around 931 eV corresponds to the  $|d^9\rangle \rightarrow |\underline{c}d^{10}\rangle$ , and thus is characteristic for the divalent

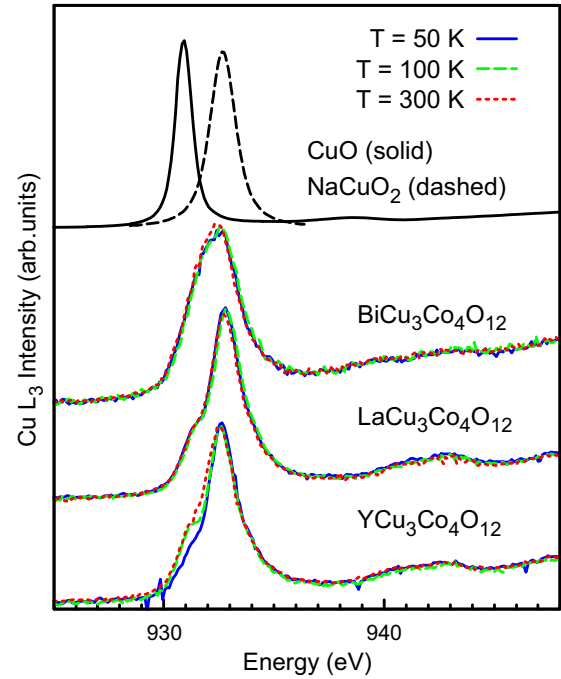


FIG. 13. Cu L<sub>3</sub> XAS spectra of the studied compounds measured in IPFY mode at 50 K (blue), 100 K (green), and 300 K (red). The XAS spectra of CuO (Cu<sup>2+</sup> reference) and NaCuO<sub>2</sub> (Cu<sup>3+</sup> reference) taken from Ref. [12] are shown for comparison.

Cu valence. Therefore, the large 933 eV feature observed in all three compounds suggests the dominant  $|d^9\bar{L}\rangle$  character of the ground state, a necessary ingredient of the Zhang-Rice

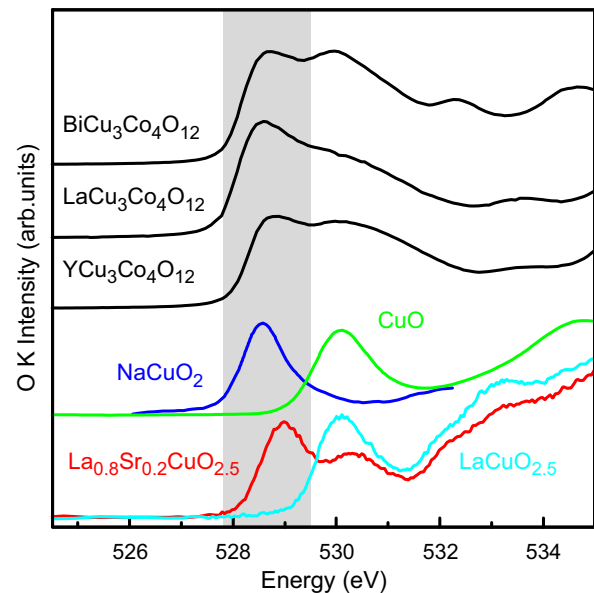


FIG. 14. O K XAS spectra of the studied compounds measured at 300 K in FY mode. The reference spectra of the pure corner-sharing ladder La<sub>0.8</sub>Sr<sub>0.2</sub>CuO<sub>2.5</sub> (Cu<sup>2.2+</sup>) taken from Ref. [64] and LaCuO<sub>2.5</sub> (Cu<sup>2+</sup>), and of the pure edge-sharing chain NaCuO<sub>2</sub> (Cu<sup>3+</sup>) are also shown for indicating the  $d^9\bar{L}$  (Zhang-Rice singlet) and  $d^9$  state in different CuO<sub>4</sub> network.

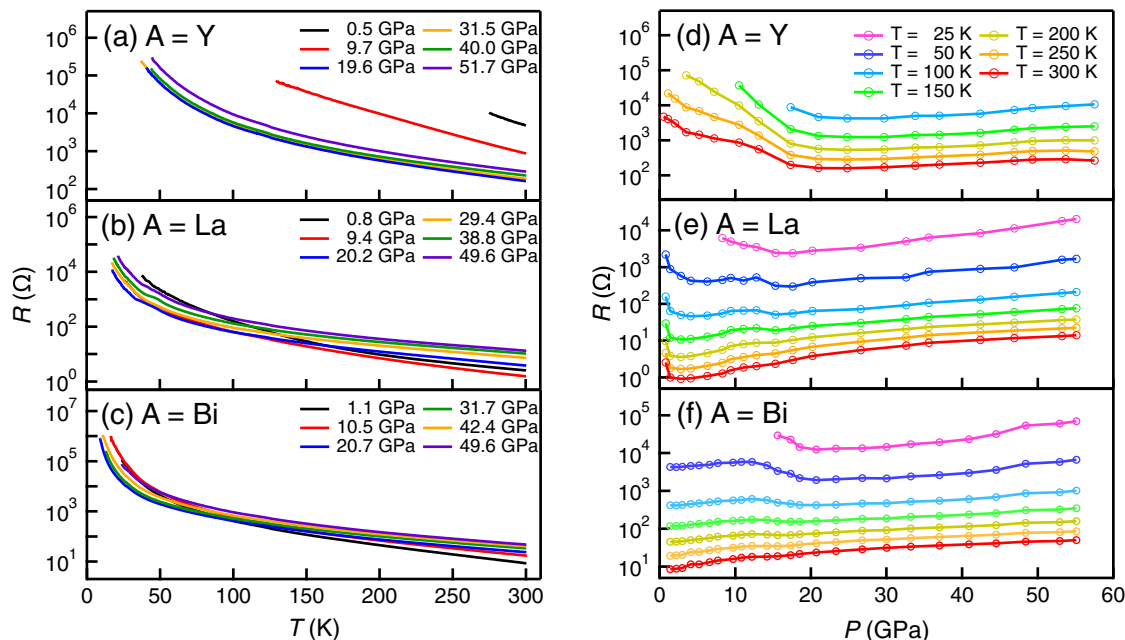


FIG. 15. Temperature ( $T$ ) dependence of electrical resistance ( $R$ ) under pressure ( $P$ ) in (a)  $YCu_3Co_4O_{12}$  (YCCO), (b)  $LaCu_3Co_4O_{12}$  (LCCO), and (c)  $BiCu_3Co_4O_{12}$  (BCCO). Pressure dependence of the electrical resistance ( $R$ ) of (d) YCCO, (e) LCCO, and (f) BCCO.

state. Furthermore, we crosscheck the Zhang-Rice singlet state at the O  $K$  edge. Figure 14 shows the O  $K$ -edge XAS for the studied compounds compared to the reference spectra for different  $CuO_4$  network. The experimental XAS spectra exhibit a clear prepeak on the low-energy side ( $\sim 528.6$  eV), highlighted by a gray shadow, which is the oxygen-specific signature for the  $|d^9 \bar{L}_z\rangle$  ground state. This peak is observed in the high-valence cuprates with the Zhang-Rice singlet ground state [see the reference spectra of  $NaCuO_2$  ( $Cu^{3+}$ ) and  $La_{0.8}Sr_{0.8}CuO_{2.5}$  ( $Cu^{2.2+}$ )]. The prepeak is absent in the divalent Cu references ( $CuO$ ,  $LaCuO_{2.5}$ ).

### E. Pressure dependence

Finally, we examine an application of pressure to YCCO, LCCO, and BCCO. Figures 15(a)–15(c) show the pressure and temperature dependence of the resistance  $R$ . Although the magnitude of  $R$  depends on the  $A$ -site elements, the resistance  $R$  of all three compounds decreases with the temperature increase, indicating an insulator-to-metal transition does not occur in the studied temperature range. In most  $3d$  transition-metal oxides, application of the physical pressure often enhances hybridization (i.e., bandwidth), and consequently the resistance is expected to decrease under pressure. Figures 15(d)–15(f) show the  $R$  vs  $P$  plot for the selected temperatures. A decreasing behavior of the resistance  $R$  is observed at low temperatures. Interestingly, the  $R$  turns into an increase at high pressures. The increase is about one order of the magnitude in the studied pressure range.

To interpret the increase of the resistance  $R$  at the elevated pressures, we simulate the crystal- and electronic-structure changes with the pressure application. To this purpose, we use the computationally cheap LDA +  $U$  scheme and search for the equilibrium atomic positions at a reduced volume within the  $A$ -site ordered perovskite crystal frame ( $Im\bar{3}$ ) for YCCO,

LCCO, and BCCO. Figure 16 summarizes the density of states calculated for the optimized structures. We find that the charge gap is increased for a reduced volume (90% of the equilibrium volume at room temperature) as a consequence of two factors: (1) the Cu–O bonding and antibonding splitting increases with

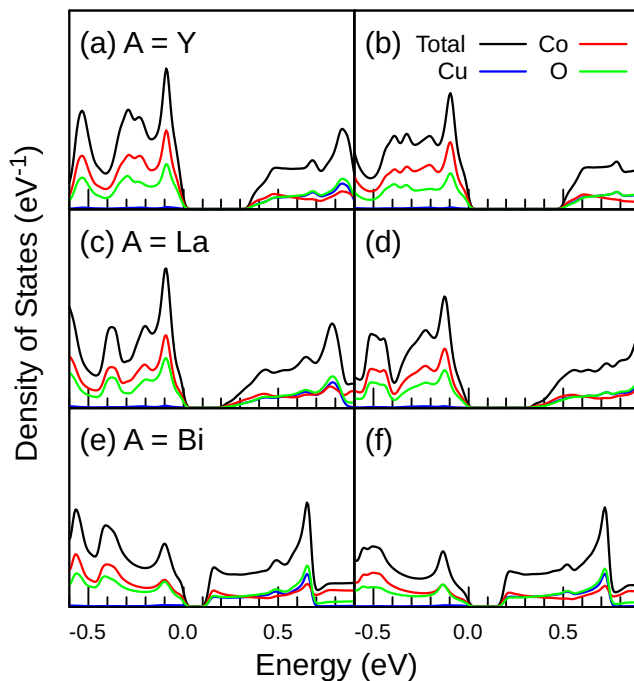


FIG. 16. The LDA +  $U$  density of states of  $ACu_3Co_4O_{12}$  calculated for (a), (c), (e) the equilibrium volume  $V_{RT}$  at room temperature in Table I and (b), (d), (f) the crystal structure optimized for the reduced volume  $V = 0.90 \times V_{RT}$ . The Fermi energy is set to zero in the panels.

a volume decrease which shifts the Cu–O antibonding peak on the conduction top toward the high-energy side, and (2) the ionic crystal-field gap of the Co ion is enhanced with the reduction of the volume. This would explain the increasing behavior of resistance  $R$  as well as the absence of the insulator-to-metal transition in YCCO, LCCO, and BCCO.

#### IV. SUMMARY

New  $A$ -site ordered perovskite oxides  $\text{LaCu}_3\text{Co}_4\text{O}_{12}$  (LCCO) and  $\text{BiCu}_3\text{Co}_4\text{O}_{12}$  (BCCO) are synthesized in high-pressure and high-temperature conditions of 12 GPa and 1273 K. We report comprehensive experimental characterization of LCCO, BCCO, and  $\text{YCu}_3\text{Co}_4\text{O}_{12}$  (YCCO) including transport and magnetization measurements, high-pressure application,  $K$ - and  $L$ -edge x-ray absorption spectroscopy, and Co  $2p$  x-ray photoemission spectroscopy. Our results suggest the valence state of  $A^{3+}\text{Cu}_3^{\sim 3+}\text{Co}_4^{\sim 3+}\text{O}_{12}^{2-}$  ( $A = \text{Y, La, Bi}$ ) with a small charge gap at ambient pressure. The trivalent Co ion has a low-spin configuration and does not show a spin-state transition in the studied temperatures (up to 300 K). Application of the physical pressure ( $\sim 55$  GPa) does not lead to an insulator-to-metal transition. The electronic structure in the ambient and elevated pressures is calculated using density-functional theory with local density approximation (LDA) plus dynamical mean-field theory (DMFT) method and with the LDA +  $U$  method, respectively. We revealed the energetics of the Co–O and Cu–O covalent-bonding formation, crystal-field splitting on the Co states, and the electronic correlation effect. This allows us to identify the mixed orbital and element character in the low-energy electronic structure

leading to the small charge gap and an unusual transport behavior at the high pressures. A comparison with a conventional perovskite cobaltite  $\text{LaCoO}_3$  using LDA provides explanation for the stable low-spin  $d^6$  configuration of the Co ion in the  $\text{ACu}_3\text{Co}_4\text{O}_{12}$  system. The Cu spin dynamics is investigated by the LDA + DMFT method. We show that a rapid screening of the Cu spin occurs largely on the isolated  $\text{CuO}_4$  plaquette, which supports the formation of the Zhang-Rice singlet state with a ligand hole, while a hybridization with the Co bands is important for fully quenching the local spin moment of Cu ( $S \sim \frac{1}{2}$ ) in a long-time response.

#### ACKNOWLEDGMENTS

A.H. was supported by JSPS KAKENHI Grants No. 21K13884, No. 21H01003, No. 23K03324, No. 23H03816, and No. 23H03817. The synchrotron experiments were performed at SPring-8 under the approval of the Japan Synchrotron Radiation Research Institute (Proposals No. 2022A1493, No. 2022B1619, No. 2022B1816). We are grateful to the KIT Light Source KARA (Karlsruhe, Germany) for the provision of beam time. We acknowledge DESY (Hamburg, Germany), a member of the Helmholtz Association HGF, for the provision of experimental facilities. Parts of this research were carried out at PETRA III. Funding for the photoemission spectroscopy instrument at beam line P04 (Contracts No. 05KS7FK2, No. 05K10FK1, No. 05K12FK1, and No. 05K13FK1 with Kiel University; Contracts No. 05KS7WW1 and No. 05K10WW2 with the University of Würzburg) by the Federal Ministry of Education and Research (BMBF) are gratefully acknowledged.

- 
- [1] Z. Zeng, M. Greenblatt, J. Sunstrom, M. Croft, and S. Khalid, *J. Solid State Chem.* **147**, 185 (1999).
- [2] Y. Long, N. Hayashi, T. Saito, M. Azuma, S. Muranaka, and Y. Shimakawa, *Nature (London)* **458**, 60 (2009).
- [3] I. Yamada, H. Etani, K. Tsuchida, S. Marukawa, N. Hayashi, T. Kawakami, M. Mizumaki, K. Ohgushi, Y. Kusano, J. Kim, N. Tsuji, R. Takahashi, N. Nishiyama, T. Inoue, T. Irifune, and M. Takano, *Inorg. Chem.* **52**, 13751 (2013).
- [4] I. Yamada, K. Shiro, H. Etani, S. Marukawa, N. Hayashi, M. Mizumaki, Y. Kusano, S. Ueda, H. Abe, and T. Irifune, *Inorg. Chem.* **53**, 10563 (2014).
- [5] I. Yamada, K. Takata, N. Hayashi, S. Shinohara, M. Azuma, S. Mori, S. Muranaka, Y. Shimakawa, and M. Takano, *Angew. Chem. Int. Ed.* **47**, 7032 (2008).
- [6] J.-G. Cheng, J.-S. Zhou, Y.-F. Yang, H. D. Zhou, K. Matsubayashi, Y. Uwatoko, A. MacDonald, and J. B. Goodenough, *Phys. Rev. Lett.* **111**, 176403 (2013).
- [7] D. Takegami, C.-Y. Kuo, K. Kasebayashi, J.-G. Kim, C. F. Chang, C. E. Liu, C. N. Wu, D. Kasinathan, S. G. Altendorf, K. Hofer, F. Meneghin, A. Marino, Y. F. Liao, K. D. Tsuei, C. T. Chen, K.-T. Ko, A. Günther, S. G. Ebbinghaus, J. W. Seo, D. H. Lee *et al.*, *Phys. Rev. X* **12**, 011017 (2022).
- [8] W.-t. Chen, Y. Long, T. Saito, J. P. Attfield, and Y. Shimakawa, *J. Mater. Chem.* **20**, 7282 (2010).
- [9] Y.-Y. Chin, H.-J. Lin, Z. Hu, Y. Shimakawa, and C.-T. Chen, *Phys. B (Amsterdam)* **568**, 92 (2019).
- [10] K. Momma and F. Izumi, *J. Appl. Crystallogr.* **44**, 1272 (2011).
- [11] I. Yamada, S. Ishiwata, I. Terasaki, M. Azuma, Y. Shimakawa, and M. Takano, *Chem. Mater.* **22**, 5328 (2010).
- [12] Y.-Y. Chin, Z. Hu, Y. Shimakawa, J. Yang, Y. Long, A. Tanaka, L. H. Tjeng, H.-J. Lin, and C.-T. Chen, *Phys. Rev. B* **103**, 115149 (2021).
- [13] I. Yamada, T. Odake, A. Tanaka, Y. Okazaki, F. Toda, Y. Ishii, T. Taniguchi, S. Kawaguchi, and A. Hariki, *Inorg. Chem.* **59**, 8699 (2020).
- [14] M. Itoh, I. Natori, S. Kubota, and K. Motoya, *J. Phys. Soc. Jpn.* **63**, 1486 (1994).
- [15] J. B. Goodenough, *J. Phys. Chem. Solids* **6**, 287 (1958).
- [16] P. Augustinský, V. Křápek, and J. Kuneš, *Phys. Rev. Lett.* **110**, 267204 (2013).
- [17] M. Kriener, C. Zobel, A. Reichl, J. Baier, M. Cwik, K. Berggold, H. Kierspel, O. Zabara, A. Freimuth, and T. Lorenz, *Phys. Rev. B* **69**, 094417 (2004).
- [18] M. Abbate, J. C. Fuggle, A. Fujimori, L. H. Tjeng, C. T. Chen, R. Potze, G. A. Sawatzky, H. Eisaki, and S. Uchida, *Phys. Rev. B* **47**, 16124 (1993).
- [19] Y. Tokura, Y. Okimoto, S. Yamaguchi, H. Taniguchi, T. Kimura, and H. Takagi, *Phys. Rev. B* **58**, R1699 (1998).

- [20] F. C. Zhang and T. M. Rice, *Phys. Rev. B* **37**, 3759 (1988).
- [21] N. B. Brookes, G. Ghiringhelli, A.-M. Charvet, A. Fujimori, T. Kakeshita, H. Eisaki, S. Uchida, and T. Mizokawa, *Phys. Rev. Lett.* **115**, 027002 (2015).
- [22] L. H. Tjeng, B. Sinkovic, N. B. Brookes, J. B. Goedkoop, R. Hesper, E. Pellegrin, F. M. F. de Groot, S. Altieri, S. L. Hulbert, E. Shekel, and G. A. Sawatzky, *Phys. Rev. Lett.* **78**, 1126 (1997).
- [23] T. Mizokawa, Y. Morita, T. Sudayama, K. Takubo, I. Yamada, M. Azuma, M. Takano, and Y. Shimakawa, *Phys. Rev. B* **80**, 125105 (2009).
- [24] D. Meyers, S. Mukherjee, J.-G. Cheng, S. Middey, J.-S. Zhou, J. B. Goodenough, B. A. Gray, J. W. Freeland, T. Saha-Dasgupta, and J. Chakhalian, *Sci. Rep.* **3**, 1834 (2013).
- [25] M. Kakihana, *J. Sol-Gel Sci. Technol.* **6**, 7 (1996).
- [26] S. Kawaguchi, M. Takemoto, K. Osaka, E. Nishibori, C. Moriyoshi, Y. Kubota, Y. Kuroiwa, and K. Sugimoto, *Rev. Sci. Instrum.* **88**, 085111 (2017).
- [27] F. Izumi and K. Momma, *Solid State Phenomena*, Vol. 130 (Trans Tech Publications, Baech, Switzerland, 2007), pp. 15–20
- [28] S. Eisebitt, T. Böske, J.-E. Rubensson, and W. Eberhardt, *Phys. Rev. B* **47**, 14103 (1993).
- [29] L. Tröger, D. Arvanitis, K. Baberschke, H. Michaelis, U. Grimm, and E. Zschech, *Phys. Rev. B* **46**, 3283 (1992).
- [30] A. J. Achkar, T. Z. Regier, H. Wadati, Y.-J. Kim, H. Zhang, and D. G. Hawthorn, *Phys. Rev. B* **83**, 129901 (2011).
- [31] A. J. Achkar, T. Z. Regier, E. J. Monkman, K. M. Shen, and D. G. Hawthorn, *Sci. Rep.* **1**, 182 (2011).
- [32] P. Blaha, K. Schwarz, G. Madsen, D. Kvasnicka, and J. Luitz, *WIEN2k, An Augmented Plane Wave + Local Orbitals Program for Calculating Crystal Properties* (Karlheinz Schwarz, Techn. Universitat Wien, Austria, 2001).
- [33] V. Křápek, P. Novák, J. Kuneš, D. Novoselov, D. M. Korotin, and V. I. Anisimov, *Phys. Rev. B* **86**, 195104 (2012).
- [34] W. Metzner and D. Vollhardt, *Phys. Rev. Lett.* **62**, 324 (1989).
- [35] A. Georges, G. Kotliar, W. Krauth, and M. J. Rozenberg, *Rev. Mod. Phys.* **68**, 13 (1996).
- [36] G. Kotliar, S. Y. Savrasov, K. Haule, V. S. Oudovenko, O. Parcollet, and C. A. Marianetti, *Rev. Mod. Phys.* **78**, 865 (2006).
- [37] A. A. Mostofi, J. R. Yates, G. Pizzi, Y.-S. Lee, I. Souza, D. Vanderbilt, and N. Marzari, *Comput. Phys. Commun.* **185**, 2309 (2014).
- [38] J. Kuneš, R. Arita, P. Wissgott, A. Toschi, H. Ikeda, and K. Held, *Comput. Phys. Commun.* **181**, 1888 (2010).
- [39] P. Werner, A. Comanac, L. de' Medici, M. Troyer, and A. J. Millis, *Phys. Rev. Lett.* **97**, 076405 (2006).
- [40] L. Boehnke, H. Hafermann, M. Ferrero, F. Lechermann, and O. Parcollet, *Phys. Rev. B* **84**, 075145 (2011).
- [41] H. Hafermann, K. R. Patton, and P. Werner, *Phys. Rev. B* **85**, 205106 (2012).
- [42] J. Kuneš, A. V. Lukoyanov, V. I. Anisimov, R. T. Scalettar, and W. E. Pickett, *Nat. Mater.* **7**, 198 (2008).
- [43] J. Kuneš, V. I. Anisimov, A. V. Lukoyanov, and D. Vollhardt, *Phys. Rev. B* **75**, 165115 (2007).
- [44] X. Wang, E. Gull, L. de' Medici, M. Capone, and A. J. Millis, *Phys. Rev. B* **80**, 045101 (2009).
- [45] M. Jarrell and J. Gubernatis, *Phys. Rep.* **269**, 133 (1996).
- [46] J. Kuneš, V. Křápek, N. Parragh, G. Sangiovanni, A. Toschi, and A. V. Kozhevnikov, *Phys. Rev. Lett.* **109**, 117206 (2012).
- [47] A. Hariki, A. Hausoel, G. Sangiovanni, and J. Kuneš, *Phys. Rev. B* **96**, 155135 (2017).
- [48] A. Hariki, M. Winder, T. Uozumi, and J. Kuneš, *Phys. Rev. B* **101**, 115130 (2020).
- [49] A. Hariki, T. Uozumi, and J. Kuneš, *Phys. Rev. B* **96**, 045111 (2017).
- [50] M. Winder, A. Hariki, and J. Kuneš, *Phys. Rev. B* **102**, 085155 (2020).
- [51] M. Ghiasi, A. Hariki, M. Winder, J. Kuneš, A. Regoutz, T.-L. Lee, Y. Hu, J.-P. Rueff, and F. M. F. de Groot, *Phys. Rev. B* **100**, 075146 (2019).
- [52] I. D. Brown and D. Altermatt, *Acta Crystallogr. B: Struct. Sci.* **41**, 244 (1985).
- [53] R. M. Wood and G. J. Palenik, *Inorg. Chem* **37**, 4149 (1998).
- [54] S. Mahapatra, J. A Halfen, E. C. Wilkinson, G. Pan, X. Wang, V. G. Young, C. J. Cramer, L. Que, and W. B. Tolman, *J. Am. Chem. Soc* **118**, 11555 (1996).
- [55] R. D. Shannon, *Acta Crystallogr. A* **32**, 751 (1976).
- [56] See Supplemental Material at <http://link.aps.org/supplemental/10.1103/PhysRevMaterials.7.073401> for Cu orbital-resolved LDA+DMFT spectra, and fitting analysis of Cu  $L_3$  XAS spectra.
- [57] R. Heikes, R. Miller, and R. Mazelsky, *Physica (Amsterdam)* **30**, 1600 (1964).
- [58] P. M. Raccah and J. B. Goodenough, *Phys. Rev.* **155**, 932 (1967).
- [59] K. Asai, A. Yoneda, O. Yokokura, J. M. Tranquada, G. Shirane, and K. Kohn, *J. Phys. Soc. Jpn.* **67**, 290 (1998).
- [60] S. Stølen, F. Grønvdold, H. Brinks, T. Atake, and H. Mori, *Phys. Rev. B* **55**, 14103 (1997).
- [61] M. W. Haverkort, Z. Hu, J. C. Cezar, T. Burnus, H. Hartmann, M. Reuther, C. Zobel, T. Lorenz, A. Tanaka, N. B. Brookes, H. H. Hsieh, H.-J. Lin, C. T. Chen, and L. H. Tjeng, *Phys. Rev. Lett.* **97**, 176405 (2006).
- [62] A. Hariki, R.-P. Wang, A. Sotnikov, K. Tomiyasu, D. Betto, N. B. Brookes, Y. Uemura, M. Ghiasi, F. M. F. de Groot, and J. Kuneš, *Phys. Rev. B* **101**, 245162 (2020).
- [63] T. Saitoh, T. Mizokawa, A. Fujimori, M. Abbate, Y. Takeda, and M. Takano, *Phys. Rev. B* **56**, 1290 (1997).
- [64] M.-J. Huang, G. Deng, Y.-Y. Chin, Z. Hu, J.-G. Cheng, F. C. Chou, K. Conder, J.-S. Zhou, T.-W. Pi, J. B. Goodenough, H.-J. Lin, and C. T. Chen, *Phys. Rev. B* **88**, 014520 (2013).
- [65] A. Hariki, A. Yamanaka, and T. Uozumi, *J. Phys. Soc. Jpn.* **84**, 073706 (2015).
- [66] D. Takegami, A. Tanaka, S. Agrestini, Z. Hu, J. Weinen, M. Rotter, C. Schüßler-Langeheine, T. Willers, T. C. Koethe, T. Lorenz, Y. F. Liao, K. D. Tsuei, H.-J. Lin, C. T. Chen, and L. H. Tjeng, *Phys. Rev. X* **13**, 011037 (2023).